



Chinese Society of Aeronautics and Astronautics  
& Beihang University

Chinese Journal of Aeronautics

cja@buaa.edu.cn  
[www.sciencedirect.com](http://www.sciencedirect.com)



FULL LENGTH ARTICLE

# Reynolds-number scaling analysis on lift generation of a flapping and passive rotating wing with an inhomogeneous mass distribution

Suyang QIN, Haotian HANG, Yang XIANG\*, Hong LIU

J. C. Wu Center for Aerodynamics, School of Aeronautics and Astronautics, Shanghai Jiao Tong University, Shanghai 200240, China

Received 5 February 2023; revised 9 May 2023; accepted 9 June 2023

## KEYWORDS

Flapping flight;  
Unsteady lift;  
Passive rotation;  
Vortex flow;  
Leading-edge vortex

**Abstract** Insects usually fly by passively rotating wings, which has been applied to the design of flapping-wing Micro-Air Vehicles (MAVs) to reduce mechanical complexity. In this paper, a robotic passive rotating-wing model is designed to investigate wing kinematics and lift generation, which are measured by a high-speed camera and a force transducer, respectively. In addition, flow fields are measured using the Particle Image Velocimetry (PIV). Experimental results demonstrate that passive rotating motion has a coordinative relationship with actively stroking motion. As the stroke amplitude or frequency increases, the rotating amplitude is enlarged. To characterize the active stroking motion, a driving Reynolds number  $Re_{\text{driving}}$  is defined, which varies from 68 to 366 in this study. Moving the gravity center of the wing towards trailing edge induces the increase of additional torque  $M$ , which decreases the wing rotating amplitude and promotes the advance of wing rotation. We find that the timing of wing rotation is gradually delayed and the mean lift coefficient  $C_L$  monotonously decreases as  $Re_{\text{driving}}$  increases. By increasing the additional torque  $M$ ,  $C_L$  is slightly improved and approaches to the lift coefficient of a real fruit fly at  $Re_{\text{driving}} \approx 230$ . The instantaneous lifts combined with the vortical structures further demonstrate that the lift generation associated with wing rotation is mainly attributed to the growth of the Leading-Edge Vortex (LEV) and the passive wake capture mechanism. Passive wake capture is influenced by LEV, reversal stroke motion and wing additional torque together, which can only maintain the lift at a high level for a considerable period. The high-lift generation mechanisms of flapping and passive rotating flight could shed light on the simplified design of MAVs and the improvement of their aerodynamic performance.

© 2023 Production and hosting by Elsevier Ltd. on behalf of Chinese Society of Aeronautics and Astronautics. This is an open access article under the CC BY-NC-ND license (<http://creativecommons.org/licenses/by-nc-nd/4.0/>).

\* Corresponding author.

E-mail address: [xiangyang@sjtu.edu.cn](mailto:xiangyang@sjtu.edu.cn) (Y. XIANG).

Peer review under responsibility of Editorial Committee of CJA.



Production and hosting by Elsevier

## 1. Introduction

Compared with fixed-wing flight, insects must flap their wings with high frequency to obtain enough lift.<sup>1,2</sup> Based on the understanding of aerodynamics of flapping flight and the moti-

vation from insect flapping flight, insect-sized flapping-wing MAVs have been successfully designed.<sup>3–8</sup> To reduce the mechanical complexity, passive wing rotation is applied in these MAVs. However, the lift of these MAVs is usually insufficient and less than that generated by real insects. To achieve the untethered flight and carry more payloads, MAV designed by Jafferis et al.<sup>6</sup> must be fitted with four wings. Aiming at these shortages and defects, it is important and valuable to explore the lift generation mechanisms of flapping and passive rotating flight in order to find effective methods to improve the aerodynamic performance of MAVs.

By considering whether wing rotation of real insects is passive without active muscle control, Bergou et al.<sup>9,10</sup> calculated the rotational power about the torsion axis based on direct numerical simulations and quasi-steady fluid force models. Their results indicate that the aerodynamic and inertial forces are sufficient to passively rotate the wings. Subsequently, Whitney and Wood<sup>11</sup> investigated the aerodynamics of passive rotation in flapping flight of a robotic model. They attempted to predict the lift and wing kinematics based on quasi-steady model. On the same robotic model, Chen et al.<sup>12</sup> experimentally explored the relationship among the formation of LEV, lift generation and wing kinematics. It is found that lift generation and wing kinematics strongly depend on active stroking motion, and the growth of LEV plays an important role in lift generation. However, these studies also point out that the unconventional lift associated with wing rotation is usually difficult to predict because of the complex unsteady mechanisms of wing rotation. Quasi-steady model cannot predict the unsteady aerodynamic forces well, let alone when the wing rotates. Thus, it is critical and urgent to investigate the unsteady lift-generation mechanisms of passive rotating and flapping wing.

The unsteady mechanisms associated with wing rotation accounting for high-lift generation have been studied for a long time. The original unsteady mechanism was identified by Weis-Fogh,<sup>13</sup> which is termed “clap-fling mechanism”. Up to now, many unsteady aerodynamic bases have been revealed, including but not limited to a stable leading-edge vortex attached on the wing,<sup>14,15</sup> wake capture,<sup>16,17</sup> delayed stall,<sup>16,19,20</sup> rotational circulation<sup>21</sup> and wing aeroelasticity.<sup>22</sup> Ground and ceiling effects are also found to promote aerodynamic forces and efficiency.<sup>23</sup> These mechanisms reveal how insects generate unconventional forces, which cannot be explained by steady-state theory. The interaction among these mechanisms accounts for the lift generation of many insects including fruit flies,<sup>16,24</sup> bees,<sup>25,26</sup> butterflies<sup>18</sup> and mosquitoes.<sup>27</sup> Moreover, the flapping flight is more efficient than the fixed-wing steady flight, which benefits from wing rotation.<sup>28</sup> Three modes of wing rotation are defined by phase shift  $\delta$  between the stroke reversal and wing rotation:<sup>16</sup> advanced, symmetrical and delayed modes. Dickinson et al.<sup>16</sup> found that phase shift has a significant role in lift generation, and insects can actively modulate the wing rotation modes during steering maneuvers. If the wing rotation is passive, it remains a question how to modulate the wing rotation mode through phase shift.

It is almost certain that insects more or less use muscles to control wing rotation. To mimic the effects of musculature, Chen et al.<sup>12</sup> designed a hinge stiffness at the wing base to affect passive wing rotation. They found that increasing hinge stiffness is beneficial to lift generation. As one of the largest

species in nature, insects have a variety of wing shapes. The mass center of the wings hardly stays on the rotational axis.<sup>29,30</sup> As a result, an additional torque is introduced, which affects the wing rotation. Moreover, Ennos<sup>29,30</sup> highlighted that the mass center of the wings is of particular importance in the design of robotic flappers. However, the effects of additional torque on wing kinematics and lift generation in a flapping and passively rotating flight are still unclear.

Passive movement widely exists in propulsion of animals, and even plays the only way for non-motile organisms to disperse.<sup>31</sup> By passively driving the motion of fins, feathers, tails and wings, animals obtain assistance and advantages to improve their locomotive performance.<sup>32,33</sup> Massive investigations have revealed that, due to flexibility and aeroelasticity, the passive deformation of wing can evidently improve the flight performance of insects, hummingbirds and bats.<sup>22,34</sup> For the hovering flight of fruit flies, they flap their wings like  $\infty$ , and the flight Reynolds number is approximately 240.<sup>16</sup> It is still a question whether a designed passively rotating wing flapper can reach the lift coefficient of a real fruit fly.

To this end, the main objective of the present experimental study is to elucidate the effects and underlying mechanisms of passive wing rotation on high-lift generation of a flapping model. This paper is organized as follows. Experimental setups and measuring methods are introduced in Section 2. Subsequently, Section 3 presents the kinematic relationship between passive rotating and active stroking motion of flapping flight. Section 4 discusses Reynolds number effects on the aerodynamic performance of the flapping and passive rotating wing. The evolution of instantaneous lift and the corresponding flow structures are studied in Section 5. Finally, brief concluding remarks are provided in Section 6 to summarize the major findings.

## 2. Materials and methods

### 2.1. Experimental setup and robotic fly model

As shown in Fig. 1(a), a robotic fly model was immersed in a glass water tank [1.2 m in length  $\times$  1.2 m in width  $\times$  2.2 m in height (2.0 m in fluid depth)]. The tank is filled up with glycerin/water mixture. The mixture density is  $1.12 \times 10^3 \text{ kg/m}^3$ , and the kinematic viscosity  $\nu$  is  $3.89 \times 10^{-5} \text{ m}^2/\text{s}$  at 20 °C temperature.

The robotic fly model has two wings, which have the identical shape used by Dickinson et al.,<sup>16</sup> as shown in Fig. 1(b) and (c). The mean wing chord  $\bar{c}$  is 86.88 mm, the wingspan  $b$  is 250 mm, the area  $S$  is 21720.76 mm<sup>2</sup>, and the aspect ratio  $AR = 4b^2/S$  is 11.5. The wing kinematics of a hovering flapping flight consists of three motions: translation (stroke), rotation (pitch), and deviation from the stroke plane (deviation). In our experiments, the wing stroke motion is driven by two waterproof servo motors, SPT 5435LV-W. The stroke velocity program is controlled by a development board, Arduino MEGA 2560. The stainless-steel stroke axis is directly installed on the output shaft of the servo. The rotation axis is fixed on the stroke axis. A low-friction deep groove ball bearing is attached to the wing rotation axis, and the wing is thereby nearly free to rotate about the rotation axis. With the aid of aerodynamic and inertia forces, the wings can passively rotate. The stroke motion in our experiments is driven by satisfying

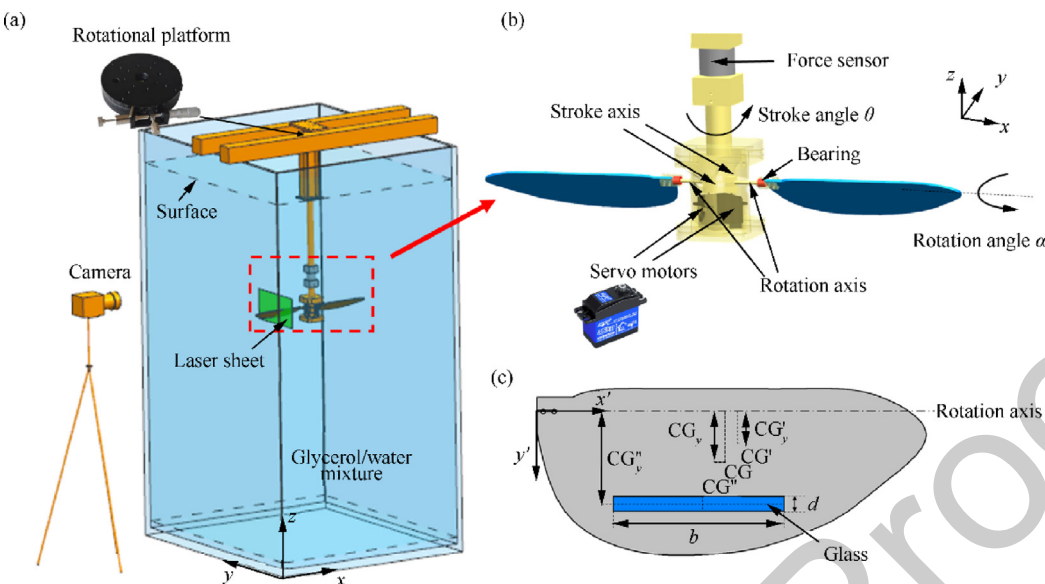


**Fig. 1** Experimental setup. (a) Schematic of the experimental setup. A robotic fly is immersed in a glass tank of glycerin/water mixture. The  $x$ - $y$ - $z$  coordinate system is the inertial system in lab. Lift  $F_l$  is in  $z$ -direction. (b) The 3D model of the robotic fly, which consists of a pair of flapping wings driven by two servo motors. (c) Construction of the wings. Two materials (distinguished by colors) with different densities are used to construct the wing.  $CG$ ,  $CG'$  and  $CG''$  are the center of gravity of the constructing wing, the center of geometry or buoyancy, and the center of the rectangular area, separately.

pure sinusoids, and the kinematics of rotating motion is experimentally measured.

The wing is 3 mm thick and mainly made of acrylic (density:  $1.19 \times 10^3$  kg/m $^3$ ). To introduce and modulate an additional torque (denoted by  $M$ ), a rectangular area of the wing is replaced by the glass with density of  $2.08 \times 10^3$  kg/m $^3$ . As shown in Fig. 1(c),  $CG$ ,  $CG'$  and  $CG''$  separately represent the gravity center of the constructing wing, the center of geometry or buoyancy, and the center of the rectangular area.  $CG_y$ ,  $CG'_y$  and  $CG''_y$  are the perpendicular distance from  $CG$ ,  $CG'$  and  $CG''$  to the wing rotation axis. By modulating the weight of the rectangular glass area and the perpendicular distance  $CG''_y$ , different additional torques are obtained. The detailed information is presented in Table 1.

## 2.2. Extraction of wing kinematics

To experimentally record the wing motion, a high-speed camera (NR 5-S2) is used. As shown in Fig. 1(a), a 10 W continuous laser sheet with a wavelength of 532 nm illuminates a vertical plane positioned at wing mid-span at stroke angle  $\theta = 0^\circ$ . The camera is mounted in front of the model, whose

central axis coincides with the wing rotation axis at  $\theta = 0^\circ$ . Twenty-five stroke periods are performed for each experiment, and the last four periods are recorded by the camera in order to obtain stable and repeatable flapping mode after several periods. The camera is thus triggered by Arduino MEGA 2560 to start recording at the beginning of the 22nd stroke period. The time-dependent position and orientation of the wing-laser intersection can be recorded. Then, we can extract the wing angles by the following three steps.

**Step 1.** The images obtained by the camera are turned to gray scale.

**Step 2.** The brightest parts indicating the wing-laser intersection can be retained using threshold division.

**Step 3.** The gradient of the line on the photograph is obtained using Hough Transform.

This process was also applied by Chen et al.<sup>12</sup>. As shown in Fig. 2(a), the wing-laser interaction and the wing root are indicated by the black line and the black point. An example of experimental laser illuminated image with wing kinematics tracking is also presented in Fig. 2(b). The wing stroke angle  $\theta$  is programmed and can also be measured in the experiments to validate the control accuracy. The equation is

**Table 1** Geometric parameters of constructing wing and additional torque.

Wing number	Mass of glass (g)	$CG_y''$ (mm)	Mass of wing (g)	$CG_y$ (mm)	$M$ (N·mm)
1	24.06	62.50	76.78	38.14	7.24
2	30.94	57.50	80.41	38.23	8.66
3	34.38	55.00	82.22	38.10	9.24
4	42.06	50.00	86.29	37.60	10.33
5	65.78	38.50	98.81	35.18	12.61

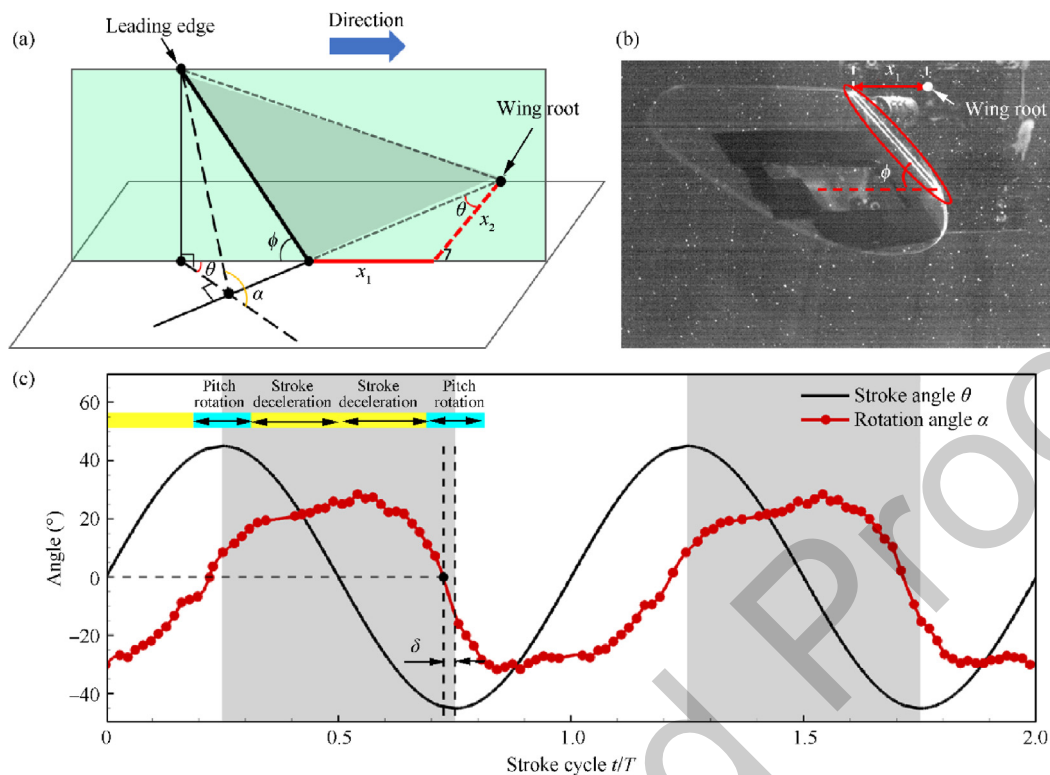


**Fig. 2** (a) Geometrical relationship between stroke angle  $\theta$  and rotation angle  $\alpha$ . The black line is the wing-laser intersection,  $\phi$  is the angle between the line of wing-laser intersection and the horizontal plane. (b) Wing kinematics tracking of  $x_1$  and  $\phi$  from a laser illuminated image. (c) Experimental kinematics extraction based on the image identification and geometrical analysis.

$$\theta = \arctan \frac{x_1}{x_2} \quad (1)$$

where  $x_1$  is the horizontal distance from wing leading edge to the root in the laser plane, and  $x_2$  is the distance from wing root to wing-laser interaction at  $\phi = 0^\circ$ . In all cases, the maximum instantaneous stroke angular error is within  $0.2^\circ$ .

According to the geometric relationship, rotation angle  $\alpha$  can be computed by

$$\alpha = \begin{cases} \arctan \frac{|\tan \phi|}{\cos \theta} & \phi > 90^\circ \\ 180^\circ - \arctan \frac{\tan \phi}{\cos \theta} & \phi < 90^\circ \\ 90^\circ & \phi = 90^\circ \end{cases} \quad (2)$$

where  $\phi$  is the angle between the line of wing-laser intersection and the horizontal plane.

According to Eq. (2), one can extract the variation of rotation angle  $\alpha$  shown in Fig. 2(c). For the wing kinematics, the phase shift  $\delta$  between the stroke reversal and wing rotation plays an important role in the generation of aerodynamic forces.<sup>[12,16]</sup> As shown in Fig. 2(c), the stroke motion is

$$\theta = \theta_{\max} \sin(2\pi ft) \quad (3)$$

where  $\theta_{\max}$  is stroke amplitude, and  $f$  is stroke frequency.  $\theta = 0^\circ$  indicates the position at the middle of stroke. As shown in Fig. 2(c), the rotation motion can be approximated as

$$\alpha = \alpha_{\max} \cos(2\pi ft + \delta) \quad (4)$$

where  $\alpha_{\max}$  is rotation amplitude. During the stroking process, Angle of Attack (AoA) of the wing is  $\text{AoA} = 90^\circ - |\alpha|$ .

In our experiments, three key parameters are controlled: stroke frequency  $f$ , stroke amplitude  $\theta_{\max}$  and additional torque  $M$ . The range of stroke frequency is 0.1–0.3 Hz, increasing by 0.1 Hz. The stroke amplitude ranges from  $45^\circ$  to  $80^\circ$ , with each increase of  $5^\circ$ . The additional torque is related to the wing geometry, which is listed in Table 1. Five kinds of wings with different additional torque are designed.

### 2.3. Instantaneous force measurement

As shown in Fig. 1(b), a force sensor is installed to hold the total weight of the robotic fly model in our experiments. The force transducer (ME DDEN-50 N) has an IP 68 protection level and range of 50 N. The sensitivity of this transducer is 0.01 N for the vertical direction, which is precise enough to measure the instantaneous lift change. The driving frequency of wing stroke is 0.1–0.3 Hz so that the lift force has a fundamental frequency of 0.2–0.6 Hz. Therefore, the lift force is collected at 100 Hz using a Multi-function Analog I.O board (NI) and filtered off-line using a zero-phase delay low-pass digital Butterworth filter with a cut-off frequency of 20 Hz. At the beginning of each measurement, the sensor is reset to zero, which removes the effects of gravity and buoyancy. Therefore, the vertical force  $F_z$  measured by the sensor is the combined result of inertial force  $ma_z$  and fluid force  $F_l$  (also lift  $L$ ), which satisfies the following expression

$$L = F_l = F_z - ma_z \quad (5)$$

where  $a_z$  is the vertical component of the wing inertial acceleration. The lift direction is vertical upwards.  $a_z$  is computed as

245  
246  
247

$$a_z = r_z [\cos(\alpha)\dot{\alpha}^2 + \sin(\alpha)\ddot{\alpha}] \quad (6)$$

248 where,  $r_z$  is the wing centroid position in vertical direction.  
249 According to the measured flapping kinematics, we apply  
250 Eq. (4) to fit the variation of  $\alpha$ , and then estimate the variation  
251 of  $a_z$  in terms of Eq. (6).

252 In general, the instantaneous and mean lift coefficients are  
253 used to characterize the aerodynamic performance of hovering  
254 flight. First, the mean lift  $\bar{L}$  in a stroke is given by

255  
256  
257

$$\bar{L} = \frac{\int_0^T L dt}{T} \quad (7)$$

258 Referring to the study of Chen et al.,<sup>12</sup> the instantaneous  
259 and mean lift coefficients ( $C_L$  and  $\bar{C}_L$ ) are defined as

260  
261  
262

$$C_L = \frac{L}{\frac{1}{2}\rho u_{rms}^2 S} \quad \bar{C}_L = \frac{\bar{L}}{\frac{1}{2}\rho u_{rms}^2 S} \quad (8)$$

263 where  $u_{rms}$  is the root mean square velocity given by

264  
265  
266

$$u_{rms} = \sqrt{\frac{1}{T} \int_0^T u^2(t) dt} \quad (9)$$

267 In Eq. (9),  $u(t)$  is the instantaneous wingtip velocity, which  
268 is approximated as a pure sinusoid based on the stroke angle  $\theta$ .  
269 The mean lift is normalized by  $\frac{1}{2}\rho u_{rms}^2 S$ , and thus the effects of  
270 wing stroke on lift generation are nearly removed. Therefore,  
271 the variation of  $\bar{C}_L$  depends on the unconventional mechanisms  
272 associated with passive wing rotation.

#### 273 2.4. Particle image velocimetry

274 Digital PIV is performed to measure the velocity fields in the  
275 slice of fluid centered on the wing. Hollow, silver-coated, neutrally  
276 buoyant glass spheres with a diameter of  $50 \pm 10 \mu\text{m}$   
277 and a density of  $1.02 \text{ g/m}^3$  are chosen as the seeding particles.  
278 The particles are illuminated by a 1.5 mm thick laser sheet projected  
279 by a 10 W continuous laser with 532 nm wavelength. A high-speed camera (NR 5-S2)  
280 is placed perpendicular to the laser sheet. In the present study, the formation of LEV is the  
281 most concerned. Thus, the measured sections should be parallel to the  $x$ - $y$  plane of the wing and are made at different spanwise locations along the wing. However, the laser sheet cannot coincide with the laser sheet all the time when the wing revolves. Thus, the method proposed by Birch and Dickinson<sup>35</sup> is applied in the present study to record the time series data at the measured section. As shown in Fig. 1(a), a rotational platform is applied to modulate the time when the laser sheet coincides with the measured section. Once the measured section coincides with the laser sheet, the high-speed camera is triggered to record a pair of images. The time interval between these two images is 5000  $\mu\text{s}$ , and the camera has a resolution of 2320 pixel  $\times$  1200 pixels with a spatial field of view of 333 mm  $\times$  170 mm. A cross-correlation of image pairs is built in TSI Insight 4G commercial software. The interrogation areas are 32 pixel  $\times$  32 pixel windows with a 50% overlap. After the velocity fields are obtained, a second-order accurate scheme is employed to calculate the vorticity fields using finite differences in velocity data with eight neighboring points. By satisfying the constraints of PIV measurements (interval time, particle size, and particle concentration), the uncertainties in

the velocity measurement and vorticity calculation are less than 1% and 3%, respectively.<sup>36,37</sup>

### 3. Passive rotating motion of flapping flight

#### 3.1. Active stroke and passive rotation motion

In our experiments, the stroke motion of the wings is actively controlled through Arduino MEGA 2560, and the rotating motion is passive with the aid of aerodynamic and wing inertial forces. Fig. 3 compares four typical wing kinematics of the robotic fly model.

First, take the case  $f = 0.1 \text{ Hz}$ ,  $\theta_{max} = 50^\circ$ ,  $M = 9.24 \text{ N-mm}$  (Fig. 3(a)) as an example to describe the change of wing angles. The stroke motion is driven by satisfying sin function, and the rotating motion is basically a cosine function. There exists phase shift  $\delta$  between the absolute peak values of stroke and rotation angles. The value of  $\delta$  is determined by the wing posture at the beginning of downstroke (labeled ② and ⑥). At the beginning of the stroke ( $t = T = 0$ , labeled ①), the rotation angle  $\alpha$  is almost at the positive peak, and thus the wing angle of attack AoA is around the minimum. At  $t = T = 0.25$ , the stroke is reversed to the downstroke period (labeled ②-④). During this process, the wing is passively rotated from positive to negative angle, and the motion is named supination. At the middle of downstroke (labeled ③), the rotation angle reaches the maximum negative value, and AoA becomes minimum again. Then, the stroke is reversed at  $t = T = 0.75$ , and the upstroke period begins. During this process, the wing passively rotates from negative to positive angle, and the motion is named pronation (process ④-⑥).

Comparing the values in Fig. 3(a) and (b), as the stroke amplitude increases from  $50^\circ$  to  $80^\circ$ , the rotation amplitude  $\alpha_{max}$  simultaneously grows from approximately  $38^\circ$  to  $50^\circ$ . Moreover, in Fig. 3(b), the rotation angle keeps zero for a short period when the wing stroke is reversed.  $\alpha = 0^\circ$  indicates that the angle of attack is  $90^\circ$ , which suggests that the fluid forces are too small to overcome the torque due to wing gravity. As the stroke frequency  $f$  increases from  $0.1 \text{ Hz}$  to  $0.3 \text{ Hz}$ , the passively rotating motion becomes smoother, as comparing between Fig. 3(a) and (c). Besides, the rotation amplitude also increases significantly from approximately  $38^\circ$  to  $63^\circ$ . When the additional torque  $M$  increases from  $9.24 \text{ N-mm}$  to  $12.61 \text{ N-mm}$ , the rotation amplitude slightly becomes larger, as comparing between Fig. 3(a) and (d).

Then, we examine the phase shift  $\delta$  between the stroke reversal and wing rotation. Three modes exist in wing rotation: advanced mode ( $\alpha < 0^\circ$  at  $t = T = 0.75$ ), symmetrical mode ( $\alpha = 0^\circ$ ), and delayed mode ( $\alpha > 0^\circ$ ). The advanced mode is identified in Fig. 3(a) and (d), where  $\delta \approx -6\%T$  and  $\delta \approx -8\%T$  respectively. In Fig. 3(b), the stroke and rotation reversal basically happen at the same time, which is in symmetrical mode. Thus, the phase shift  $\delta$  is approximately zero. In Fig. 3(c), the rotation process is in delayed mode, and  $\delta$  is about  $11\%T$ .

#### 3.2. Coordinative relationship between active stroke and passive rotation

According to Fig. 3, there are some internal connections between the active stroke and passive rotation motions. Thus,

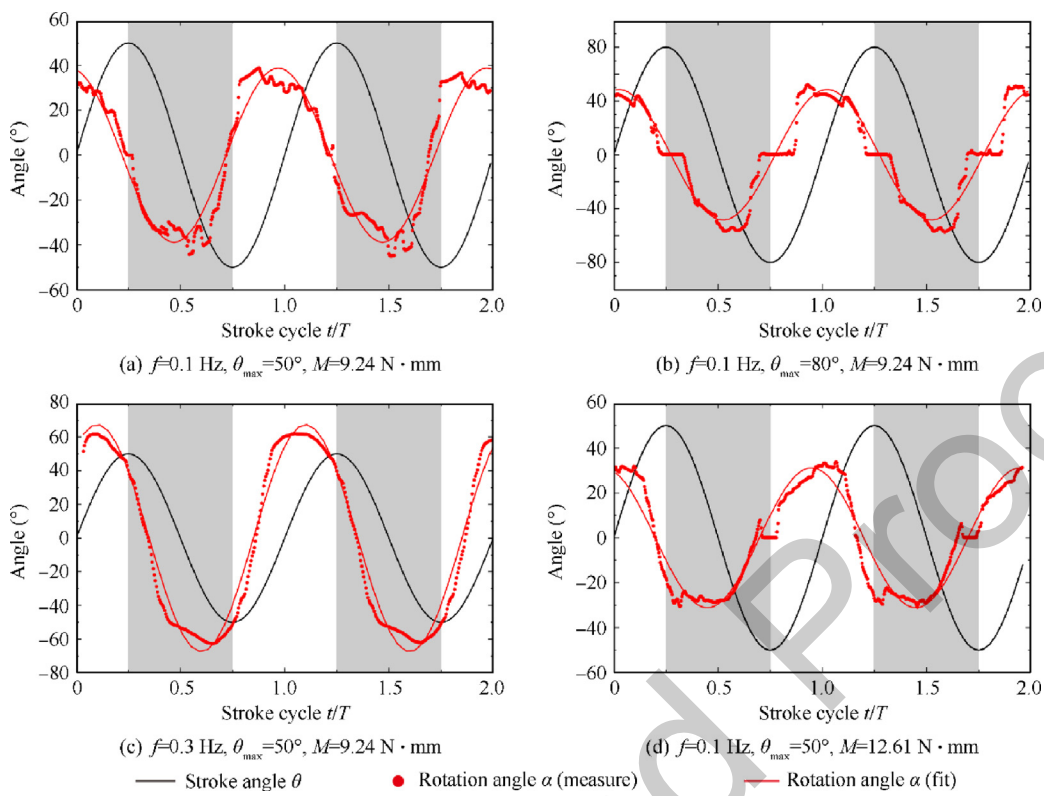


Fig. 3 Wing kinematics of robotic fly model.

we further investigate the relationship between stroke amplitude  $\theta$  and rotation amplitude  $\alpha$ , which is presented in Fig. 4(a). There exist two laws in their relationship, first, the rotation amplitude exhibits a nearly linear increase with the stroke amplitude for different flapping frequencies  $f$  and additional torques  $M$ ; secondly, the rotation amplitude increases with the flapping frequency, while becomes smaller as the additional torque increases. Based on the rotation amplitude and the time spent by wing rotation, the averaged rotation velocity  $\omega_{\text{rotation}}$  can be estimated. The relationship between the rotation velocity and the stroke amplitude is presented in Fig. 4(b). It is found that the rotation velocity strongly depends on the frequency, while it is weakly related to the stroke amplitude and additional torque.

By referring to the studies of Dickinson et al.,<sup>16</sup> the stroke motion can be characterized by driving Reynolds number, which is expressed as

$$Re_{\text{driving}} = \frac{4\pi b^2 f A_{\text{stroke}}}{ARv} \quad (10)$$

where  $A_{\text{stroke}}$  is the stroke amplitude in radius and satisfies  $A_{\text{stroke}} = \theta_{\text{max}} = 180^\circ$ , and  $v$  is the kinematic viscosity. According to Eq. (10), driving Reynolds number depends on the translational velocity of wingtip, which is determined by stroke amplitude and frequency. It is widely known that the phase shift  $\delta$  plays an important role in the generation of aerodynamic forces. Thus, the variation of phase shift  $\delta$  against the driving Reynolds number is examined and shown in Fig. 5. The driving Reynolds number varies from 68 to 122 for  $f = 0.1$  Hz, from 122 to 244 for  $f = 0.2$  Hz, and 205 to 366 for  $f = 0.3$  Hz. These driving Reynolds numbers basically

cover the Reynolds number range of insect hovering flight. Phase shift  $\delta$  increases as  $Re_{\text{driving}}$  grows for a fixed additional torque  $M$ . This tendency indicates that as the stroke frequency increases, the passive wing rotation will be significantly delayed with respect to the active stroke reverse. In addition,  $\delta$  has a decreasing tendency with increasing additional torque  $M$ , which indicates that  $M$  is helpful to advance the wing rotation. Moreover, the advanced mode  $\delta < 0$  only happens when  $Re_{\text{driving}}$  is smaller than approximately 100. As  $Re_{\text{driving}}$  increases,  $\delta$  does not monotonously grow, and instead nearly arrives a peak at  $Re_{\text{driving}} \approx 250$ . Then,  $\delta$  slightly decreases with  $Re_{\text{driving}}$  when  $Re_{\text{driving}}$  is larger than 250.

#### 4. Reynolds-number effects on aerodynamic performance of passive rotation and flapping wing

High-lift generation is one of the most fascinating features in insect hovering flight. Fig. 6 illustrates the variation of time-averaged lift coefficient  $\bar{C}_L$  in a cycle against driving Reynolds number  $Re_{\text{driving}}$ . It is an obvious tendency that  $\bar{C}_L$  generally decreases with increasing  $Re_{\text{driving}}$ . Moreover, the growing torque  $M$  causes  $\bar{C}_L$  to increase. For a fixed stroke frequency, the decreased tendency of  $\bar{C}_L$  shows an approximately linear relationship with  $Re_{\text{driving}}$ . Moreover, either the growth of driving Reynolds number or decrease of additional torque can lead to the increase of phase shift  $\delta$ , as shown in Fig. 5. The wing rotation changes from the advanced mode to the delayed mode. As a result, the mean lift is reduced. The effect of phase shift  $\delta$  on the lift generation has been well studied<sup>16,17</sup>. Based on the analysis of the relationship between averaged lift and driving

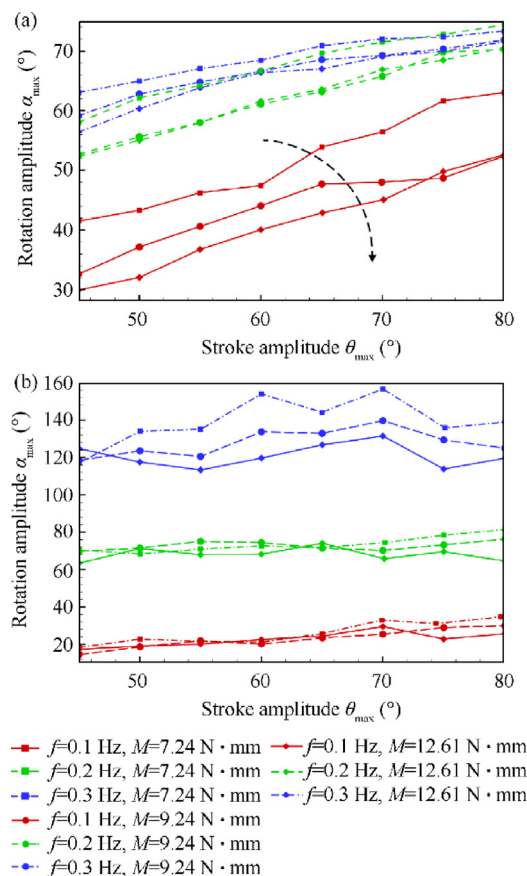


**Fig. 4** (a) Rotating amplitude as function of actively controlled kinematic parameters; (b) rotating velocity as function of actively controlled kinematic parameters.

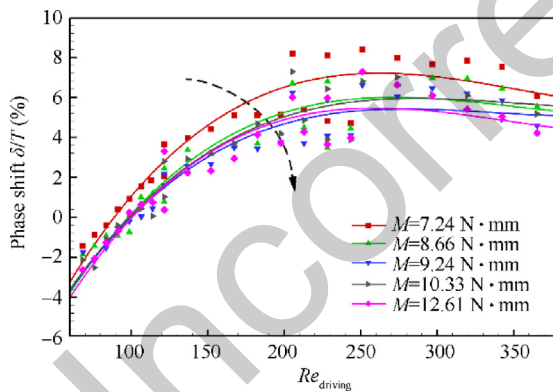


**Fig. 5** Phase shift  $\delta$  as function of driving Reynolds number  $Re_{\text{driving}}$  for different additional torque  $M$ .

Reynolds number, increasing the additional torque  $M$  is helpful to enhance lift, which suggests a potential design principle for the wing mass distribution of robotic fly. The detailed instantaneous lift evolution and flow structures of passive rotating wings will be presented and discussed in Section 5.

According to the real wing kinematics of a hovering fruit fly measured by Fry et al.,<sup>38</sup> the driving Reynolds number is approximately  $Re_{\text{driving}} = 235$  and the mean lift coefficient is approximately 0.38 based on the estimated fruit fly weight.

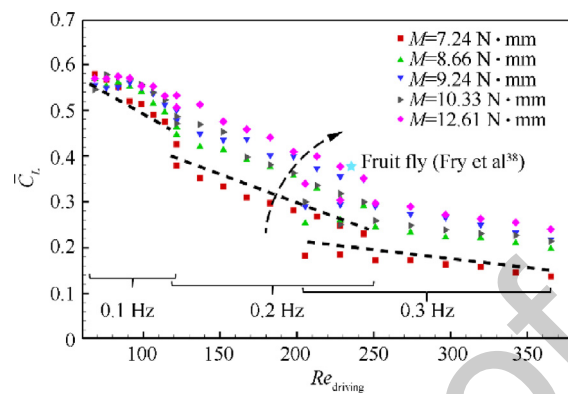


**Fig. 6** Variation of mean lift coefficient  $\bar{C}_L$  in a cycle against driving Reynolds number  $Re_{\text{driving}}$  for wings with different additional torques  $M$ . The blue star indicates the result of fruit fly measured by Fry et al.<sup>38</sup> The dashed lines indicate the tendency of  $\bar{C}_L$  with  $Re_{\text{driving}}$  for different stroke frequencies.

In Fig. 6, it is observed that the mean lift of fruit fly is close to that of the passive robotic fly for  $f = 0.2$  Hz,  $\theta_{\max} = 75^\circ$ ,  $M = 12.61$  N·mm, corresponding to  $Re_{\text{driving}} \approx 230$ . This agreement suggests and supports two implications. First, the wing rotating motion must be assisted by the muscle in hovering flight of fruit fly in order to obtain enough lift to support its weight. Secondly, the mass distribution of wing should generate an additional torque, which plays a positive role in lift generation.

As the driving Reynolds number  $Re_{\text{driving}}$  increases from 70 to 375, the time-averaged lift  $\bar{C}_L$  decreases from 0.58 to 0.14. This tendency suggests that passive locomotion is an effective means of propulsion at low Reynolds number, while the effect becomes less obvious as Reynolds number increases.

## 5. Lift force and flow structures of passive rotating wings

The instantaneous lift forces and the corresponding detailed flow structures can reveal the underlying mechanisms of passive rotating wings. Three typical cases are selected and compared, which show the effects of driving Reynolds number and addition torque. Fig. 7(a)–(c) present the measured instantaneous lift force in two flapping cycles. It is shown that the instantaneous lift presents a good periodicity. Figs. 8 and 9 show the typical flow structures of these cases.

Fig. 7(a) shows the evolution of instantaneous lift for the case  $f = 0.1$  Hz,  $\theta_{\max} = 80^\circ$ ,  $M = 9.24$  N·mm. The wing motion is in symmetric mode. Besides, Fig. 8 shows the evolution of vorticity contours at the middle wingspan location of this case. In Fig. 7(a), as  $t/T$  changes from 0 to 0.15, the unconventional lift increases significantly, and AoA of the wing is relatively large. According to the wing kinematics in Fig. 3(b), the period  $t/T = 0\text{--}0.15$  is stroke deceleration phase, during which the LEV grows and stably maintains on the wing upper surface (Fig. 8(a) and (b)). Thus, it results in high instantaneous lift. During  $t/T = 0.15\text{--}0.25$ , the wing rotates to the vertical status, and AoA gradually approaches  $90^\circ$ . However, the instantaneous lift does not decrease rapidly, but still maintains a relatively large value. At the stroke end, the stroking velocity approaches zero, resulting in the phenomenon that

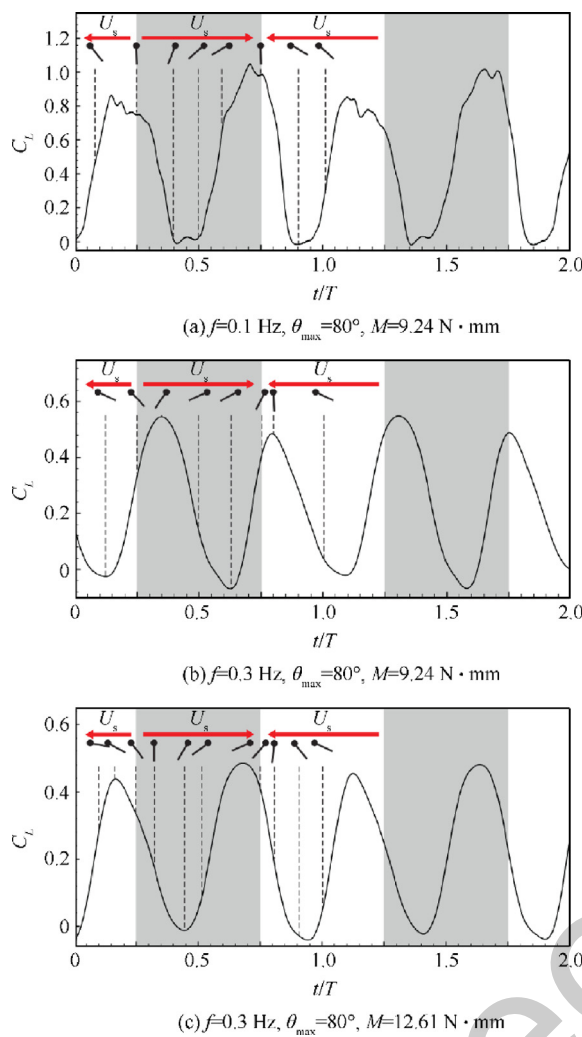


**Fig. 7** Evolution of measured instantaneous lift. The gray regions are the downstroke periods, and the white regions are the upstroke. The black rods represent the positions and AoAs of the wing, and black circles are the wing leading edges. The red lines with arrows indicate the stroke directions.

the conventional lift depending on forward speed is negligible. Thus, unconventional forces play dominant roles in lift generation and enhancement. First, rotational circulation (akin to the Magnus effect) contributes to the increase of the lift during this period. Secondly, as shown in Fig. 8(b) and (c), LEVs remain closely attached to the wing at the upstroke end ( $t/T = 0.25$ ), which generate a vortex-enhanced lift. These mechanisms are generally found in the studies on insect flapping wing flight.<sup>14,15,18,20</sup> The flow pattern at  $t/T = 0.25$  (Fig. 8(c)) together with the continuous large instantaneous lift (Fig. 7(a)) suggests a passive wake capture mechanism at the stroke end, which contributes to the maintenance of high-lift. Different from the wake capture observed by Dickinson et al.<sup>16</sup>, passive wake capture cannot generate another lift-peak during or after wing rotation, but just maintains the lift at a high level with the aid of LEV. The passive rotating motion is caused by the combination of stroke motion and flow structure. The wing has to adapt to the vortical structures and cannot capture the leading-edge vortex like active wing

rotating motion; thus, it is influenced by LEV, reversal stroke motion and wing additional torque together.

As  $t/T$  changes from 0.25 to 0.5, the stroke velocity is accelerated, while the instantaneous lift decreases. As shown in Fig. 8(c) and (d), the wing undergoes a deep stall, whose AoA changes from  $90^\circ$  to  $60^\circ$ , and the vorticity on the upper wing surface is still small. As  $t/T$  changes from 0.5 to 0.75, a new LEV generates and rapidly grows to attach to the wing surface (Fig. 8(d) and (e)), and the instantaneous lift is recovered in Fig. 7(a). From  $t/T = 0.75$  to  $t/T = 1.0$ , upstroke process of the wing begins, and the wing passively rotates, which results in the decreasing instantaneous lift. Based on the above description and analysis, the high-lift generation in the flapping and passively rotating flight is largely owing to the growth and attachment of LEV, rotational circulation and passive wake capture mechanism. The first two aspects are similar to those of active flapping wing, while the last one needs to comprehensively consider the flow structure and additional torque of the wing.

Fig. 7(b) shows the evolution of the instantaneous lift for  $f = 0.3 \text{ Hz}, \theta_{\max} = 80^\circ, M = 9.24 \text{ N} \cdot \text{mm}$ , which is in delayed mode. In the stroke deceleration phase ( $t/T = 0-0.25$  and  $0.5-0.75$ ), the instantaneous lift bottoms out and rises until the stroke reverses. The relative low lift during this phase is attributed to the small wing AoA and stroke deceleration. The lift increase is caused by two reasons: the growth of LEV with increasing AoA and rotational circulation. As shown in Fig. 9(b), the size of LEV is much smaller than that in Fig. 9(a), because the wing AoA is quite small in the middle of stroke for  $f = 0.3 \text{ Hz}$ . Owing to the small size of LEV, the passive wake capture during the wing rotation is simultaneously weak. As a result, lift cannot maintain at a high level after the peaks, and decreases rapidly during the passive rotation process. Fig. 7(c) shows the evolution of instantaneous lift for  $f = 0.3 \text{ Hz}, \theta_{\max} = 80^\circ, M = 12.61 \text{ N} \cdot \text{mm}$ . As the additional torque  $M$  increases from  $9.24 \text{ N} \cdot \text{mm}$  to  $12.61 \text{ N} \cdot \text{mm}$ , the maximum instantaneous lift value is advanced from  $t/T = 0.37$  to  $t/T = 0.18$ . As shown in Fig. 7(c), the instantaneous lift arrives at the peak value before the stroke reverses. Besides, the wing passively rotates approximately from  $t/T = 0.18$  to  $t/T = 0.5$ . During this rotating process, the lift decreases rapidly. By comparing Fig. 9(b) and (c), the wing AoAs are both small, resulting in small LEV sizes. Therefore, the contribution of LEV growth and passive wake capture to lift generation should also be limited.

To summarize the above analysis on instantaneous lifts and flow structures, driving Reynolds number strongly affects the phase shift. As a result, the formation of LEV is limited as the phase shift becomes larger. Rotational circulation always exists in the rotating motion of the wings in the reciprocating strokes. The above two mechanisms have been discovered in the previous works.<sup>12,16,17</sup> Compared with the wake capture only controlled by active rotating motion, passive wake capture is influenced by LEV, reversal stroke motion and wing additional torque together, and its impact is significant when  $\delta \leq 0$  or  $\delta$  is a small positive value.

Based on the performance of passive flapping wings in vortical structures and instantaneous and averaged lifts, we can speculate that the wing rotation of the small-size insects (such as larva) is close to passive locomotion during hovering flight. Medium-size insects (such as mosquito or fruit fly) can passively rotate their wings with the aid of wing muscle in order

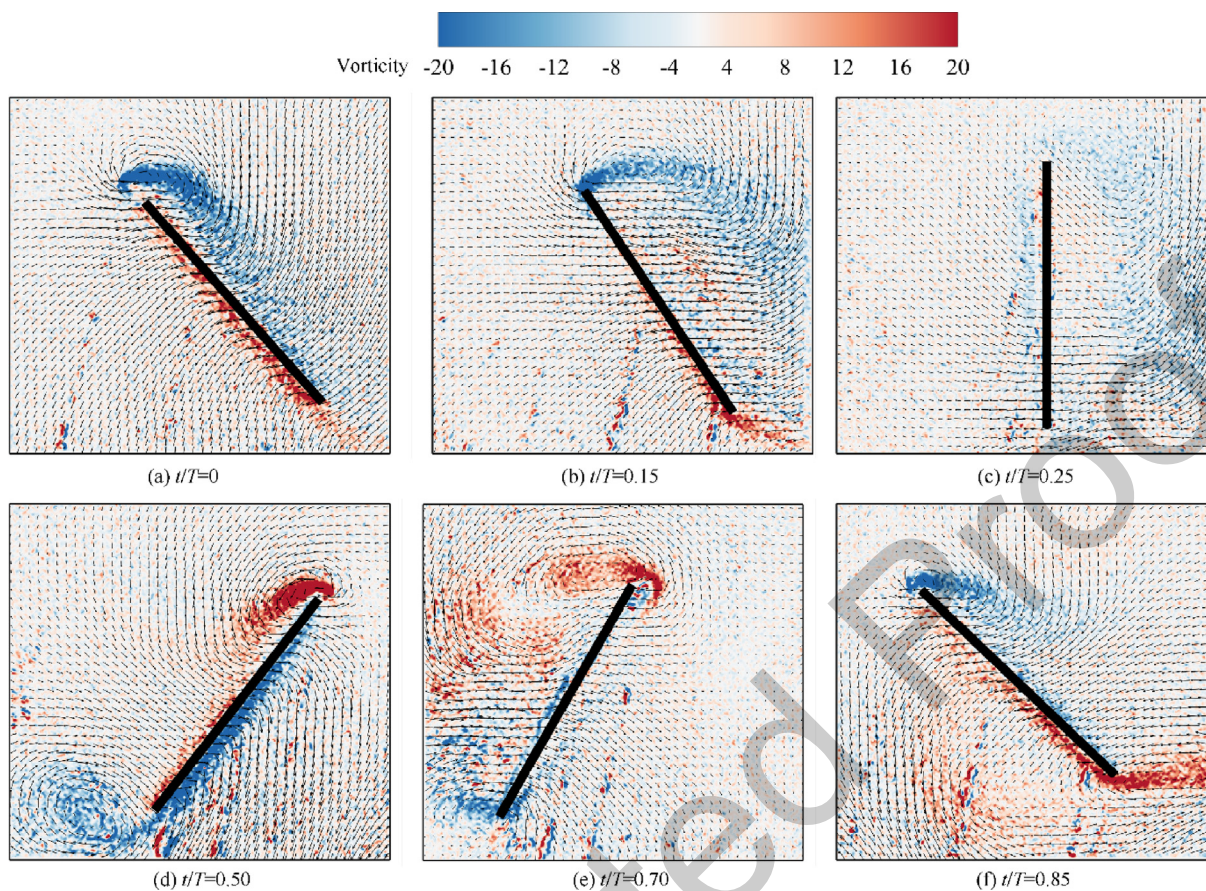


**Fig. 8** Vorticity contours around the wing for  $f = 0.1$  Hz,  $\theta = 80^\circ$ ,  $M = 9.24$  N·mm. (a)-(f) show the flow contours at different instants. The measured section is the spanwise location at the middle of the wingspan. The solid lines indicate the position and attack angle of the wing.

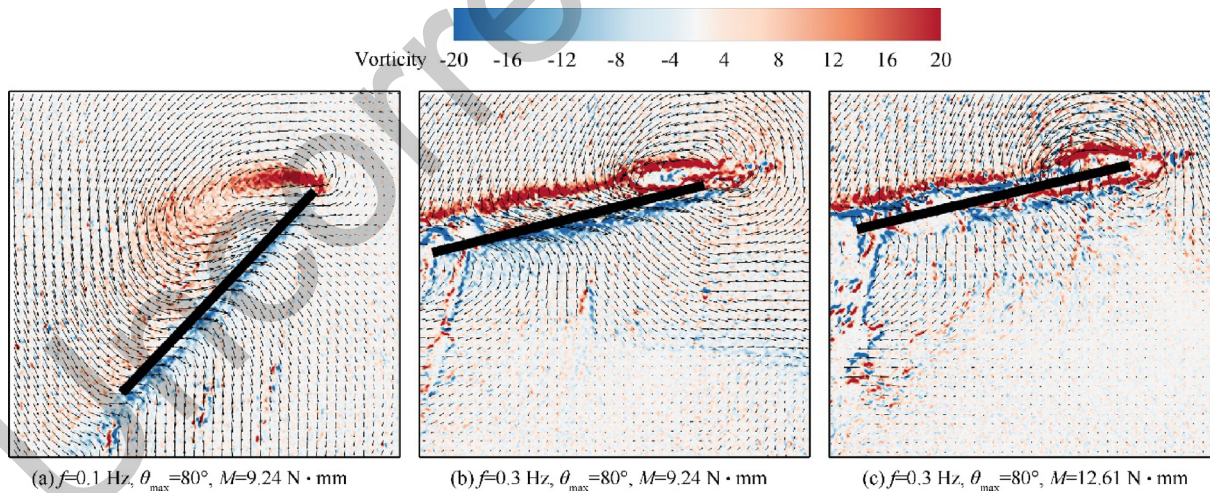


**Fig. 9** Vorticity contours at the middle of downstroke ( $t/T = 0.5$ ) around wing for (a)  $f = 0.1$  Hz,  $\theta_{\max} = 80^\circ$ ,  $M = 9.24$  N·mm; (b)  $f = 0.3$  Hz,  $\theta_{\max} = 80^\circ$ ,  $M = 9.24$  N·mm; and (c)  $f = 0.3$  Hz,  $\theta_{\max} = 80^\circ$ ,  $M = 12.61$  N·mm.

546 to efficiently enhance lift. In contrast, large-scale insects (such  
547 as dragonfly) and hummingbirds have to actively control the  
548 wing rotation with the aid of musculature and aerodynamic  
549 forces to generate high lift.

## 6. Conclusions

In this paper, a robotic fly model with flapping and passively rotating wings is designed to investigate the coordinative wing

553 motion and lift generation mechanisms. The wing has an inhomogeneous mass distribution. By adjusting the gravity center  
554 of the wing, different additional torques, which affect the wing  
555 kinematics, are obtained. Wing kinematics is experimentally  
556 extracted through the images recorded by high-speed camera.  
557 Instantaneous lift is measured by a high-precision transducer,  
558 and flow fields are measured using PIV technique. By analyzing  
559 the wing kinematics and instantaneous lift, the main conclusions  
560 are as follows:

- 562 (1) A coordinative relationship between active stroking and  
563 passive rotating motion is demonstrated. With the aid of  
564 aerodynamic and wing inertial forces, the wing is passively rotated. The rotation amplitude becomes larger  
565 as the stroke amplitude and frequency increases, while it gets smaller as the additional torque increases. Moreover,  
566 the phase shift  $\delta$  between wing rotation and stroke reversal depends on active stroking motion. A driving  
567 Reynolds number  $Re_{driving}$  is defined to characterize the active stroking motion. As  $Re_{driving}$  increases,  $\delta$   
568 increases before  $Re_{driving}$  arrives approximately 250. Moreover,  $\delta < 0$  is obtained when  $Re_{driving} < 100$ . In  
569 addition,  $\delta$  decreases when the additional torque  
570 increases for a fixed  $Re_{driving}$ .
- 571 (2) The aerodynamic performance of flapping and passive  
572 rotating wing becomes weaker as  $Re_{driving}$  increases. Based on the instantaneous lift, the mean lift coefficient  
573  $\bar{C}_L$  is estimated.  $\bar{C}_L$  decreases as  $Re_{driving}$  increases, and  
574  $\bar{C}_L$  slightly increases by enhancing the additional torque.  
575 This tendency suggests a potential principle for designing the wing of a robotic flapper. Moreover, it is also  
576 suggested that passive locomotion is efficient at low  
577 Reynolds number, but are of weak effect at high Reynolds  
578 number.
- 579 (3) The unsteady mechanisms generated by passive wing  
580 rotation enhance the instantaneous lift. The peak lift is  
581 closely related to the wing rotation. According to the  
582 evolution of flow patterns, the high-lift generation can  
583 be largely attributed to the growth of the leading-edge  
584 vortex (LEV), rotational circulation and passive wake  
585 capture mechanism. Compared with the wake capture  
586 mechanism observed by Dickinson et al.,<sup>16</sup> passive wake  
587 capture is influenced by LEV, reversal stroke motion  
588 and wing additional torque together. It can only maintain  
589 the lift at a high level for a considerable period,  
590 rather than generate another lift peak.

#### 599 Declaration of competing interest

600 The authors declare that they have no known competing  
601 financial interests or personal relationships that could have  
602 appeared to influence the work reported in this paper.

#### 603 Acknowledgments

604 This work was supported by the National Nature Science  
605 Foundation of China (12102259, 12202273) and the China  
606 Postdoctoral Science Foundation (2018M642007).

#### References

1. Sun M. Insect flight dynamics: stability and control. *Rev Mod Phys* 2014;**86**(2):615–46.
2. Bin Abas MF, Bin Mohd Rafie AS, Bin Yusoff H, et al. Flapping wing micro-aerial-vehicle: kinematics, membranes, and flapping mechanisms of ornithopter and insect flight. *Chin J Aeronaut* 2016;**29**(5):1159–77.
3. Wang L, Song BF, Sun ZC, et al. Review on ultra-lightweight flapping-wing nano air vehicles: artificial muscles, flight control mechanism, and biomimetic wings. *Chin J Aeronaut* 2023;**36**(6):63–91.
4. Lentink D, Jongerius SR, Bradshaw NL. The scalable design of flapping micro-air vehicles inspired by insect flight. In: Flying insects and robots. Berlin: Springer; 2009. p. 185–205.
5. Ma KY, Chirarattananon P, Fuller SB, et al. Controlled flight of a biologically inspired, insect-scale robot. *Science* 2013;**340**(6132):603–7.
6. Jafferis NT, Helbling EF, Karpelson M, et al. Untethered flight of an insect-sized flapping-wing microscale aerial vehicle. *Nature* 2019;**570**(7762):491–5.
7. Dong X, Li DC, Xiang JW, et al. Design and experimental study of a new flapping wing rotor micro aerial vehicle. *Chin J Aeronaut* 2020;**33**(12):3092–9.
8. Wang SQ, Song BF, Chen A, et al. Modeling and flapping vibration suppression of a novel tailless flapping wing micro air vehicle. *Chin J Aeronaut* 2022;**35**(3):309–28.
9. Bergou AJ, Xu S, Wang ZJ. Passive wing pitch reversal in insect flight. *J Fluid Mech* 2007;**591**:321–37.
10. Bergou AJ, Ristroph L, Guckenheimer J, et al. Fruit flies modulate passive wing pitching to generate in-flight turns. *Phys Rev Lett* 2010;**104**(14):148101.
11. Whitney JP, Wood RJ. Aeromechanics of passive rotation in flapping flight. *J Fluid Mech* 2010;**660**:197–220.
12. Chen YF, Gravish N, Desbiens AL, et al. Experimental and computational studies of the aerodynamic performance of a flapping and passively rotating insect wing. *J Fluid Mech* 2016;**791**:1–33.
13. Weis-Fogh T. Quick estimates of flight fitness in hovering animals, including novel mechanisms for lift production. *J Exp Biol* 1973;**59**(1):169–230.
14. Ellington CP. Aerodynamics and the origin of insect flight. *Adv Insect Physiol* 1991;**23**:171–210.
15. Ellington CP, van den Berg C, Willmott AP, et al. Leading-edge vortices in insect flight. *Nature* 1996;**384**(6610):626–30.
16. Dickinson MH, Lehmann FO, Sane SP. Wing rotation and the aerodynamic basis of insect flight. *Science* 1999;**284**(5422):1954–60.
17. Xiang Y, Hang HT, Qin SY, et al. Scaling analysis of the circulation growth of leading-edge vortex in flapping flight. *Acta Mechanica Sinica* 2021;**37**(10):1530–43.
18. Srygley RB, Thomas ALR. Unconventional lift-generating mechanisms in free-flying butterflies. *Nature* 2002;**420**(6916):660–4.
19. Dickinson MH, Götz KG. Unsteady aerodynamic performance of model wings at low Reynolds numbers. *J Exp Biol* 1993;**174**(1):45–64.
20. Corke TC, Thomas FO. Dynamic stall in pitching airfoils: aerodynamic damping and compressibility effects. *Annu Rev Fluid Mech* 2015;**47**:479–505.
21. Ellington CP. The aerodynamics of hovering insect flight i–iv. *Philos Trans R Soc London Ser B* 1984;**305**:1–181.
22. Shyy W, Kang CK, Chirarattananon P, et al. Aerodynamics, sensing and control of insect-scale flapping-wing flight. *Proc R Soc A* 2016;**472**(2186):20150712.
23. Hao JJ, Zhang YL, Zhou C, et al. Aerodynamic performance of hovering micro revolving wings in ground and ceiling effects at low Reynolds number. *Chin J Aeronaut* 2023;**36**(1):152–65.

- 673 24. Sun M, Wu JH. Aerodynamic force generation and power  
674 requirements in forward flight in a fruit fly with modeled wing  
675 motion. *J Exp Biol* 2003;206(Pt 17):3065–83.
- 676 25. Engels T, Kolomenskiy D, Schneider K, et al. Bumblebee flight in  
677 heavy turbulence. *Phys Rev Lett* 2016;116(2):028103.
- 678 26. Ravi S, Kolomenskiy D, Engels T, et al. Bumblebees minimize  
679 control challenges by combining active and passive modes in  
680 unsteady winds. *Sci Rep* 2016;6:35043.
- 681 27. Bompfrey RJ, Nakata T, Phillips N, et al. Smart wing rotation  
682 and trailing-edge vortices enable high frequency mosquito flight.  
683 *Nature* 2017;544(7648):92–5.
- 684 28. Pesavento U, Wang ZJ. Flapping wing flight can save aerody-  
685 namic power compared to steady flight. *Phys Rev Lett* 2009;103  
686 (11):118102.
- 687 29. Ennos AR. The importance of torsion in the design of insect  
688 wings. *J Exp Biol* 1988;140(1):137–60.
- 689 30. Ennos AR. The inertial cause of wing rotation in Diptera. *J Exp*  
690 *Biol* 1988;140(1):161–9.
- 691 31. Dickinson MH, Farley CT, Full RJ, et al. How animals move: An  
692 integrative view. *Science* 2000;288(5463):100–6.
32. Fish FE, Lauder GV. Passive and active flow control by swimming  
fishes and mammals. *Annu Rev Fluid Mech* 2006;38:193–224.
33. Ramananarivo S, Godoy-Diana R, Thiria B. Rather than reso-  
nance, flapping wing flyers may play on aerodynamics to improve  
performance. *PNAS* 2011;108(15):5964–9.
34. Kang CK, Aono H, Cesnik CES, et al. Effects of flexibility on the  
aerodynamic performance of flapping wings. *J Fluid Mech*  
2011;689:32–74.
35. Birch JM, Dickinson MH. The influence of wing–wake interac-  
tions on the production of aerodynamic forces in flapping flight. *J*  
*Exp Biol* 2003;206(13):2257–72.
36. Xiang Y, Qin SY, Liu H. Patterns for efficient propulsion during  
the energy evolution of vortex rings. *Eur J Mech Fluids*  
2018;71:47–58.
37. Xiang Y, Li ZQ, Qin SY, et al. Formation number and pinch-off  
signals of disc vortex ring based on a Lagrangian analysis. *Exp*  
*Therm Fluid Sci* 2021;129:110452.
38. Fry SN, Sayaman R, Dickinson MH. The aerodynamics of free-  
flight maneuvers in *Drosophila*. *Science* 2003;300(5618):495–8.